Development of a modal reduced-order model of xenon oscillations in PWRs

Downloaded from: https://research.chalmers.se, 2026-11-07 16:34 UTC

Citation for the original published paper (version of record):
Pedersen, K., Demaziere, C., Vinai, P. (2027). Development of a modal reduced-order model of xenon oscillations in PWRs. Progress in Nuclear Energy, 202.
http://dx.doi.org/10.1016/j.pnucene.2026.106605

N.B. When citing this work, cite the original published paper.

research.chalmers.se offers the possibility of retrieving research publications produced at Chalmers University of Technology. It covers all kind of research output: articles, dissertations, conference papers, reports etc. since 2004. research.chalmers.se is administrated and maintained by Chalmers Library

(article starts on next page)

Progress in Nuclear Energy 202 (2027) 106605

Contents lists available at ScienceDirect

Progress in Nuclear Energy

journal homepage: www.elsevier.com/locate/pnucene

Development of a modal reduced-order model of xenon oscillations in PWRs

Kristoffer Tofveson Pedersen *, Christophe Demazière, Paolo Vinai

Chalmers University of Technology, Department of Physics, Division of Subatomic, High Energy and Plasma Physics, 41296, Gothenburg, Sweden

ARTICLE INFO

Keywords:
Reduced order modelling
Xenon oscillations
Multi-group diffusion theory
Modal decomposition

ABSTRACT

This work presents a modal reduced-order modelling approach to predict the stability of xenon oscillations in large Pressurised Water Reactors (PWRs). The model, labelled 2G-HET, is developed and compared to a simplified model (2G-HOM). The 2G-HET model takes the two-energy group and three-dimensional macroscopic cross sections, homogenised at the assembly or sub-assembly level, as well as the reactor geometry, as input. It calculates spatial eigenmodes and their coupled time-dependent amplitudes for neutron flux, iodine, and xenon concentrations. In contrast, the 2G-HOM model uses cross sections homogenised over the entire core-reflector region and analytically calculated eigenmodes.

The 2G-HOM and 2G-HET are compared against each other based on simulated cross-section data from the Ringhals-4 PWR in Sweden. The analysis shows the significant influence of mode coupling on power and axial offset deviations, with 2G-HET capturing detailed spatial dynamics absent in 2G-HOM. Specifically, the heterogeneous treatment reveals couplings between even and odd modes, not present in the homogeneous model. In a case study, the 2G-HET model showed stable decaying oscillations with modal periods in the interval $[31.5; 39.3]$ h. Comparisons with 2G-HOM over a range of power feedback coefficient strengths (FB-scaling) show similar asymptotic behaviour between the two models. However, 2G-HOM have an onset of stable oscillations at 25% lower FB-scaling value compared to 2G-HET. It also consistently displays faster decaying oscillations compared to 2G-HET.

The results highlight that high spatial resolution plays an important role when simulating xenon oscillations following reactor perturbations using three dimensional modal expansion models. The findings show that 2G-HET captures more features of the system, which substantially alters the stability prediction and mode-coupling behaviour. Capturing these features has potential applications in ensuring safe and flexible reactor operation by capturing more complex dynamics of xenon oscillations which cannot be reproduced in simpler models.

1. Introduction

Xenon-135, the most potent known thermal neutron absorber, is produced in power reactors partly as a fission product but primarily through the decay of iodine-135. In large reactors, the delayed production and decay of xenon-135 within the core can lead to oscillations in the spatial distribution of power following asymmetrical perturbations to the neutron flux. These oscillations – denoted xenon oscillations – may exhibit divergent behaviour in certain reactor core configurations, requiring operator intervention to prevent unsafe power peaking and potential fuel overheating (U.S. Department of Energy, 1993; U.S. Nuclear Regulatory Commission, 2011; Utley, 1972; Graves, 1970).

The global share of solar and wind energy in the electricity mix has increased to 13% worldwide in the past thirty years, with large variability between individual countries (Ritchie and Rosado, 2020). The intermittency of these electricity sources and the decline in shares of other flexible electricity sources create challenges in the balance of the electricity grid. One proposed solution is to change the mode of operation in large thermal Light Water Reactors (LWRs) from producing base-load power to flexible load-following production (Hjelmeland et al., 2025; International Atomic Energy Agency, 2018; Persson et al., 2012; OECD/NEA, 2021).

Core control during load-following operations in large power reactors might lead to the development of xenon oscillations. Thus, xenon oscillations may be more frequent in the future, when more intermittent energy sources are introduced. For this reason, it is imperative to assess the stability regarding xenon oscillations for a given core configuration to avoid possible divergent oscillations altogether (Peakman et al., 2020; International Atomic Energy Agency, 2018).

Given the challenges posed by xenon-induced instabilities, several neutron transport models have been developed to study xenon oscillations effectively. These models may include stochastic Monte Carlo methods or deterministic methods. Stochastic methods provide a high

* Correspondence to: Blåsebergavägen 20 lgh 1104, 21633 Malmö, Sweden.
E-mail addresses: kriped@chalmers.se (K.T. Pedersen), demaz@chalmers.se (C. Demazière), vinai@chalmers.se (P. Vinai).

https://doi.org/10.1016/j.pnucene.2026.106605
Received 8 October 2025; Received in revised form 23 May 2026; Accepted 8 September 2026
Available online 22 September 2026
0149-1970/© 2026 The Authors. Published by Elsevier Ltd. This is an open access article under the CC BY license (http://creativecommons.org/licenses/by/4.0/).

level of accuracy (Kitcher and Chirayath, 2017; Mazaher et al., 2020; Chang, 2016) but have the drawback of being prohibitively resource-expensive for modelling the extended time scales of xenon oscillations across many core configurations. Commercial core simulators based on deterministic methods, such as nodal diffusion codes, offer a more computationally feasible alternative and are widely used in reactor analysis and operational planning (Yarbrough et al., 1997). Simpler analytical descriptions in one dimension have also been employed (Song and Cho, 1997; Song et al., 1999; Zarei et al., 2017; Kobayashi and Yoshikuni, 1982), though these methods might not be able to capture the full range of behaviour of a three-dimensional core.

In addition to the above, other classes of techniques can be used. For instance, Modal Reduced Order Modelling (ROM) aims to simplify solving high-dimensional partial differential equations (PDEs) by projecting them onto a lower-dimensional subspace of spatial modes. This, in turn, results in a truncated small number of coupled ordinary differential equations (ODEs) to be solved to create an approximation of the full system dynamics (Carreño et al., 2019; Demazière, 2017). A notable feature of this method is the access to the time-dependence of individual modes, which improves the physical insights gained from the analysis.

The modal ROM method based on both eigenmodes, as well as modes based on Proper Orthogonal Decomposition, has been utilised with success in describing instabilities in Boiling Water Reactors (BWR) (G. Verdú and Miró, 1998; Hennig et al., 2019).

This work utilises a λ-eigenmode expansion-based modal ROM to simulate the xenon behaviour of a three-dimensional heterogeneous two-group core system based on a set of equilibrium macroscopic cross-sections. The method is based on previous one-dimensional analytical models without coupling investigated by Song and Cho (1997), Song et al. (1999) and Christie and Poncelet (1973). The method of modal reduced order modelling of xenon oscillations is also described in the textbooks of Bell and Glasstone (1970) and Lee (2020). The effect of mode coupling is investigated in analytical one-dimensional models by Norinder (1963), Gyorey (1962) and Canosa and Brooks (1966). A higher number of modes was considered analytically by Lellouche (1962) and in numerical calculations by Kalkkuhl and Döring (1993), who included the effect of core control and power feedback. The novelty of this paper is the investigation of the evolution of eigenmodes extended to a more refined nodal three-dimensional two-energy group system than what has been investigated earlier. Also, the employed xenon model includes coupling between higher-order modes and modelling of the power coefficient of reactivity. This investigation is complemented by an analytical analysis of the mode stability without the effect of coupling and a thorough analysis of the effect of homogenisation. The extension of the ROM model to three dimensions and greater spatial resolution might allow for greater flexibility and applicability when modelling xenon oscillations with potentially complex initial conditions.

The model, referred to as 2G-HET, uses three-dimensional steady-state heterogeneous macroscopic cross section data in two energy groups and the physical dimensions of the reactor to predict xenon-iodine dynamics in the core. A feedback term based on homogenised cross-sections is added to the underlying equations to simulate the power coefficient of reactivity. The 2G-HET model predicts the temporal evolution of amplitudes of multiple spatial eigenmodes related to xenon and iodine concentration deviations and neutron flux deviations for multiple spatial eigenmodes, offering enhanced resolution of coupled mode dynamics. The model is tested for its ability to predict deviations in power and axial offset following externally induced axial perturbations using generated cross sections based on core data from the Ringhals-4 PWR in Sweden. Mode couplings are shown to play a significant role in predicting the power and axial offset deviations. A second model, referred to as 2G-HOM, is employed to assess the impact of homogenisation on stability predictions. For this purpose, 2G-HOM is first compared to existing literature, the two models are then compared in terms of eigenvalues, the behaviour of the modes without coupling, feedback response, coupling strengths and decay characteristics of the axial offset of the power.

The paper is structured as follows. First, the 2G-HET model and subsequent data analysis methods are explained in detail. Second, the case study data from the Ringhals-4 PWR, as well as the values of physical parameters, are introduced. Third, the 2G-HET model simulates the time evolution of flux, iodine and xenon concentration in the core. Fourth, thorough data analysis is carried out, studying the effects of mode coupling on the resulting power and axial offset deviations as well as on mode behaviour. Lastly, the 2G-HOM is introduced, and the results of this model are compared to those of the 2G-HET to assess the effects of homogenisation. The extension of the ROM model to three dimensions and greater spatial resolution might allow for greater flexibility and applicability when modelling xenon oscillations with potentially complex initial conditions.

2. Developed ROM methodology

2.1. Derivation of the modal reduced order model

The general methodology for deriving the modal ROM involves the following steps to simplify the system dynamics while retaining its essential features for analysis. First, the stationary forward and adjoint neutron balance equations in two energy groups, alongside the iodine and xenon balance equations, are formulated. This is done to determine equilibrium conditions and provide a basis for studying perturbations in the reactor core. Next, the PDEs that describe the time-dependent behaviour of the system are introduced. Finally, the λ-eigenmode expansion is applied, which is thoroughly described in the works of Carreño et al. (2019, 2017), Verdú et al. (1994), Velarde et al. (1978). This method reduces the complexity of the high-dimensional PDEs to a manageable set of ODEs, which capture the lower-order behaviour of neutron flux and iodine and xenon concentration dynamics.

The following approximations are introduced:

- The tellurium decay is assumed to be instantaneous due to its short half-life.
- The two-group diffusion approximation is applied as it is suitable for low-leakage thermal reactors.
- Upscattering is neglected due to its minimal impact on thermal systems.
- Only linear terms are included in the dynamic equations as only small changes in neutron flux are needed to assess the stability of the system with respect to spatial xenon oscillations.
- Neutron absorption in xenon is assumed only in the thermal energy group where the capture cross section is much larger.

With these approximations, the stationary balance equations for the neutron flux, iodine, and xenon concentrations are written in matrix form as follows:

$$[\mathbf{D}(\mathbf{r})\nabla^2 + \boldsymbol{\Sigma}^{woX}(\mathbf{r}) - \tilde{\mathbf{T}}_{th}\sigma_{a,X}X_{eq}(\mathbf{r})] \times \hat{\boldsymbol{\Phi}}_{eq}(\mathbf{r}) + \frac{1}{k_{eff}}\mathbf{F}(\mathbf{r}) \times \hat{\boldsymbol{\Phi}}_{eq}(\mathbf{r}) = \begin{pmatrix} 0 \\ 0 \end{pmatrix} \quad (1)$$

$$\hat{T}_f \cdot \frac{\gamma_I}{\nu k_{eff}}\mathbf{F}(\mathbf{r}) \times \hat{\boldsymbol{\Phi}}_{eq}(\mathbf{r}) - \lambda_I I_{eq}(\mathbf{r}) = 0 \quad (2)$$

$$\lambda_I I_{eq}(\mathbf{r}) + \hat{T}_f \cdot \frac{\gamma_X}{\nu k_{eff}}\mathbf{F}(\mathbf{r}) \times \hat{\boldsymbol{\Phi}}_{eq}(\mathbf{r}) - \lambda_X X_{eq}(\mathbf{r}) - \hat{T}_f \cdot \sigma_{a,X}X_{eq}(\mathbf{r})\hat{\boldsymbol{\Phi}}_{eq}(\mathbf{r}) = 0 \quad (3)$$

where $I_{eq}(\mathbf{r})$ is the iodine concentration and $X_{eq}(\mathbf{r})$ is the xenon concentration, λ_l and γ_l are the decay constant and branching ratio of species l (iodine and xenon). $\sigma_{a,X}$, ν, and k_{eff} are the xenon microscopic absorption cross section, the average number of neutrons emitted per fission event and the effective multiplication factor, respectively. The matrices and vectors in the equations are defined as:

$$\hat{\boldsymbol{\Phi}}_{eq}(\mathbf{r}) = \begin{bmatrix} \phi_{eq,1}(\mathbf{r}) \\ \phi_{eq,2}(\mathbf{r}) \end{bmatrix} \quad \boldsymbol{\Sigma}^{woX}(\mathbf{r}) = \begin{bmatrix} -\Sigma_{a,1}(\mathbf{r}) - \Sigma_r(\mathbf{r}) & 0 \\ \Sigma_r(\mathbf{r}) & -\Sigma_{a,2}^{woX}(\mathbf{r}) \end{bmatrix} \quad \mathbf{T}_{th} = \begin{bmatrix} 0 & 1 \\ 0 & 0 \end{bmatrix}$$

$$\hat{T}_f = \begin{bmatrix} 1 & 0 \end{bmatrix} \qquad \mathbf{F}(\mathbf{r}) = \begin{bmatrix} \nu\Sigma_{f,1}(\mathbf{r}) & \nu\Sigma_{f,2}(\mathbf{r}) \\ 0 & 0 \end{bmatrix}$$

$$\tilde{\mathbf{T}}_{th} = \begin{bmatrix} 0 & 0 \\ 0 & 1 \end{bmatrix} \qquad \mathbf{D}(\mathbf{r}) = \begin{bmatrix} -D_1(\mathbf{r}) & 0 \\ 0 & -D_2(\mathbf{r}) \end{bmatrix}$$

According to standard notation, $\Sigma_{\alpha,g}$ is the macroscopic cross section for the reactions α and group g, D_g is the diffusion coefficient for group g, ϕ_g is the neutron scalar flux for group g, $\Sigma_{a,2}$ and $\Sigma_{a,2}^{woX}$ are the macroscopic thermal absorption cross section with and without the contribution from the xenon-135 content, respectively. From Eqs. (2) and (3), the equilibrium iodine and xenon concentrations can be derived as:

$$I_{eq}(\mathbf{r}) = \hat{T}_f \cdot \frac{\gamma_I}{\nu k_{eff} \lambda_I} \mathbf{F}(\mathbf{r}) \times \hat{\boldsymbol{\Phi}}_{eq}(\mathbf{r}) \tag{4}$$

$$X_{eq}(\mathbf{r}) = \frac{\lambda_I I_{eq}(\mathbf{r}) + \hat{T}_f \cdot \frac{\gamma_X}{\nu k_{eff}} \mathbf{F}(\mathbf{r}) \times \hat{\boldsymbol{\Phi}}_{eq}(\mathbf{r})}{\lambda_X + \sigma_{a,X} \phi_{eq,2}(\mathbf{r})} \tag{5}$$

The adjoint solution to Eq. (1) is labelled with the dagger symbol and satisfies the following relation for a generic matrix $\mathbf{A}(\mathbf{r})$:

$$\left\langle \hat{\boldsymbol{\Phi}}^{\dagger}(\mathbf{r}) \middle| \mathbf{A}(\mathbf{r}) \times \hat{\boldsymbol{\Phi}}(\mathbf{r}) \right\rangle = \left\langle \mathbf{A}^{\dagger}(\mathbf{r}) \times \hat{\boldsymbol{\Phi}}^{\dagger}(\mathbf{r}) \middle| \hat{\boldsymbol{\Phi}}(\mathbf{r}) \right\rangle \tag{6}$$

with the inner product defined as:

$$\left\langle \hat{\Psi}(\mathbf{r}) \middle| \hat{\boldsymbol{\Phi}}(\mathbf{r}) \right\rangle = \int_V \hat{\Psi}(\mathbf{r}) \cdot \hat{\boldsymbol{\Phi}}(\mathbf{r}) d^3\mathbf{r} = \int_V (\psi_1(\mathbf{r})\phi_1(\mathbf{r}) + \psi_2(\mathbf{r})\phi_2(\mathbf{r})) d^3\mathbf{r} \tag{7}$$

The adjoint diffusion problem for the equilibrium neutron flux is written as:

$$[\nabla \cdot \mathbf{D}(\mathbf{r})\nabla + \boldsymbol{\Sigma}^{T,woX}(\mathbf{r}) - \tilde{\mathbf{T}}_{th}\sigma_{a,X} X_{eq}(\mathbf{r})] \times \hat{\boldsymbol{\Phi}}^{\dagger}_{eq}(\mathbf{r}) = \frac{1}{k^{\dagger}_{eff}} \mathbf{F}(\mathbf{r}) \times \hat{\boldsymbol{\Phi}}^{\dagger}_{eq}(\mathbf{r}) \tag{8}$$

The solution to the adjoint equation plays a key role in constructing the ROM model by providing necessary orthogonality conditions.

The forward problem is an λ-eigenvalue problem with infinitely many solutions in the form of eigenvalue-eigenmode pairs, which all satisfy the following relation:

$$[\nabla \cdot \mathbf{D}(\mathbf{r})\nabla + \boldsymbol{\Sigma}^{woX}(\mathbf{r}) - \tilde{\mathbf{T}}_{th}\sigma_{a,X} X_{eq}(\mathbf{r})] \times \hat{\boldsymbol{\Phi}}_n(\mathbf{r}) = \frac{1}{\lambda_n} \mathbf{F}(\mathbf{r}) \times \hat{\boldsymbol{\Phi}}_n(\mathbf{r}); \quad n = 0, 1, 2, \ldots \tag{9}$$

The spatial eigenmodes ϕ_n are ordered such that the corresponding real eigenvalues go from the largest to the smallest, i.e., $\lambda_0 > \lambda_1 > \lambda_2 > \cdots$. The eigenvalue λ_0 associated with the fundamental eigenmode ϕ_0 is then equal to the effective multiplication factor k_{eff}.

For the eigenmodes of the system, the following orthogonality relation holds between the adjoint and the forward eigenmodes (Carreño et al., 2017):

$$\left\langle \hat{\boldsymbol{\Phi}}^{\dagger}_n(\mathbf{r}) \middle| \mathbf{F}(\mathbf{r}) \times \hat{\boldsymbol{\Phi}}_m(\mathbf{r}) \right\rangle = \left\langle \mathbf{F}^T(\mathbf{r}) \times \hat{\boldsymbol{\Phi}}^{\dagger}_n(\mathbf{r}) \middle| \hat{\boldsymbol{\Phi}}_m(\mathbf{r}) \right\rangle \tag{10}$$

$$= \delta_{nm} \left\langle \hat{\boldsymbol{\Phi}}^{\dagger}_n(\mathbf{r}) \middle| \mathbf{F}(\mathbf{r}) \times \hat{\boldsymbol{\Phi}}_m(\mathbf{r}) \right\rangle \quad n, m = 0, 1, 2, \ldots$$

Having established the stationary system, the time-dependent system is described as follows:

$$\mathbf{v}^{-1} \frac{\partial \hat{\boldsymbol{\Phi}}(\mathbf{r},t)}{\partial t} = \left[\nabla \cdot \mathbf{D}(\mathbf{r})\nabla + \boldsymbol{\Sigma}^{woX}(\mathbf{r}) - \tilde{\mathbf{T}}_{th}\sigma_{a,X} X(\mathbf{r},t) + \frac{1}{k_{eff}} \mathbf{F}(\mathbf{r})\right] \times \hat{\boldsymbol{\Phi}}(\mathbf{r},t) \tag{11}$$

$$+ \mathbf{K}_{th} \times (\hat{\boldsymbol{\Phi}}(\mathbf{r},t) - \hat{\boldsymbol{\Phi}}_{eq}(\mathbf{r}))$$

$$\frac{\partial I(\mathbf{r},t)}{\partial t} = \hat{T}_f \cdot \frac{\gamma_I}{\nu k_{eff}} \mathbf{F}(\mathbf{r}) \times \hat{\boldsymbol{\Phi}}(\mathbf{r},t) - \lambda_I I(\mathbf{r},t) \tag{12}$$

$$\frac{\partial X(\mathbf{r},t)}{\partial t} = \lambda_I I(\mathbf{r},t) + \hat{T}_f \cdot \left(\frac{\gamma_X}{\nu k_{eff}} \mathbf{F}(\mathbf{r}) - \mathbf{T}_{th}\sigma_{a,X} X(\mathbf{r},t)\right) \times \hat{\boldsymbol{\Phi}}(\mathbf{r},t) \tag{13}$$

$$- \lambda_X X(\mathbf{r},t)$$

Where it is assumed that cross sections variations are in the thermal absorption cross section alone and due to changes in xenon concentration. In Eq. (11) the matrix $\mathbf{K}_{th}$ of power coefficients of reactivity is introduced. This matrix is based on differences in reaction rates between two power levels and is fully explained in Section 4.2.1. The velocity matrix is also introduced:

$$\mathbf{v}^{-1} = \begin{bmatrix} v_1^{-1} & 0 \\ 0 & v_2^{-1} \end{bmatrix} \tag{14}$$

The neutron flux, iodine and xenon concentrations are split into their stationary equilibrium values and the time- and space-dependent fluctuations (denoted as $\delta\phi, \delta I$ and δX) as:

$$\hat{\boldsymbol{\Phi}}(\mathbf{r},t) = \hat{\boldsymbol{\Phi}}_{eq}(\mathbf{r}) + \delta\hat{\boldsymbol{\Phi}}(\mathbf{r},t) \tag{15}$$

$$I(\mathbf{r},t) = I_{eq}(\mathbf{r}) + \delta I(\mathbf{r},t) \tag{16}$$

$$X(\mathbf{r},t) = X_{eq}(\mathbf{r}) + \delta X(\mathbf{r},t) \tag{17}$$

Inserting Eqs. (15) to (17) into (11) to (13), subtracting the stationary Eqs. (1) to (3) and neglecting non-linear terms, the balance equations for the fluctuations of the different variables then read as:

$$\mathbf{v}^{-1} \frac{\partial \delta\hat{\boldsymbol{\Phi}}(\mathbf{r},t)}{\partial t} = \Big[\nabla \cdot \mathbf{D}(\mathbf{r})\nabla + \boldsymbol{\Sigma}^{woX}(\mathbf{r}) \tag{18}$$

$$- \tilde{\mathbf{T}}_{th}\sigma_{a,X} X_{eq}(\mathbf{r}) + \mathbf{K}_{th} + \frac{1}{k_{eff}} \mathbf{F}(\mathbf{r}) \Big] \times \delta\hat{\boldsymbol{\Phi}}(\mathbf{r},t)$$

$$- \tilde{\mathbf{T}}_{th}\sigma_{a,X} \hat{\boldsymbol{\Phi}}_{eq}(\mathbf{r}) \delta X(\mathbf{r},t)$$

$$\frac{\partial \delta I(\mathbf{r},t)}{\partial t} = \hat{T}_f \cdot \frac{\gamma_I}{\nu k_{eff}} \mathbf{F}(\mathbf{r}) \times \delta\hat{\boldsymbol{\Phi}}(\mathbf{r},t) - \lambda_I \delta I(\mathbf{r},t) \tag{19}$$

$$\frac{\partial \delta X(\mathbf{r},t)}{\partial t} = \lambda_I \delta I(\mathbf{r},t) \tag{20}$$

$$+ \hat{T}_f \cdot \left[\frac{\gamma_X}{\nu k_{eff}} \mathbf{F}(\mathbf{r}) - \mathbf{T}_{th}\sigma_{a,X} X_{eq}(\mathbf{r})\right] \times \delta\hat{\boldsymbol{\Phi}}(\mathbf{r},t)$$

$$- \left[\lambda_X + \sigma_{a,X}\phi_{eq,2}(\mathbf{r})\right] \delta X(\mathbf{r},t)$$

The truncated λ-eigenmode expansion decomposes the spatial distribution of flux, iodine, and xenon into a weighted sum of N spatial modes with time-dependent amplitudes such as:

$$\delta\hat{\boldsymbol{\Phi}}(\mathbf{r},t) \approx \sum_{n=0}^{N} P_n(t) \hat{\boldsymbol{\Phi}}_n(\mathbf{r}) \tag{21}$$

$$\delta I(\mathbf{r},t) \approx \hat{T}_f \cdot \sum_{n=0}^{N} Q_n \mathbf{F}(\mathbf{r}) I_n(t) \times \hat{\boldsymbol{\Phi}}_n(\mathbf{r}) \tag{22}$$

$$\delta X(\mathbf{r},t) \approx \hat{T}_f \cdot \sum_{n=0}^{N} Q_n \mathbf{F}(\mathbf{r}) X_n(t) \times \hat{\boldsymbol{\Phi}}_n(\mathbf{r}) \tag{23}$$

In the expansion of δI and δX, $\mathbf{F}(\mathbf{r})$ is used to get the correct orthogonality properties and the scaling factor $Q_n = \frac{\left\langle \hat{\boldsymbol{\Phi}}^{\dagger}_n(\mathbf{r}) \middle| \hat{\boldsymbol{\Phi}}_n(\mathbf{r}) \right\rangle}{\left\langle \hat{\boldsymbol{\Phi}}^{\dagger}_n(\mathbf{r}) \middle| \mathbf{F}(\mathbf{r}) \times \hat{\boldsymbol{\Phi}}_n(\mathbf{r}) \right\rangle}$ is needed to get the correct units of concentration cm^{-3}.

These eigenmodes represent different spatial configurations of the neutron flux of the reactor. Eqs. (21)–(23) are inserted in the partial differential Eqs. (19)–(21). Then, each term of the equations is multiplied by the adjoint mode $\hat{\boldsymbol{\Phi}}^{\dagger}_m$ with $m = 0, 1, 2, \ldots$ and integrated over the reactor volume. Considering the orthogonality property Eq. (11), the resulting equations are then a set of $3N$ coupled ordinary differential equations, i.e.:

$$\frac{\mathrm{d}P_m(t)}{\mathrm{d}t} = -\frac{1}{\Lambda_m}\left(\frac{1}{\lambda_m} - \frac{1}{\lambda_0}\right) P_m(t) \tag{24}$$

$$+ \frac{1}{\Lambda_m} \sum_{n=0}^{N} \frac{\left\langle \hat{\boldsymbol{\Phi}}^{\dagger}_m(\mathbf{r}) \middle| \mathbf{K}_{th} \times \hat{\boldsymbol{\Phi}}_n(\mathbf{r}) \right\rangle}{\left\langle \hat{\boldsymbol{\Phi}}^{\dagger}_m(\mathbf{r}) \middle| \mathbf{F}(\mathbf{r}) \times \hat{\boldsymbol{\Phi}}_m(\mathbf{r}) \right\rangle} P_n(t)$$

$$- \frac{\sigma_{a,X}}{\Lambda_m} \sum_{n=0}^{N} Q_n \frac{\left\langle \hat{\boldsymbol{\Phi}}^{\dagger}_m(\mathbf{r}) \middle| \phi_{eq,2}(\mathbf{r}) \mathbf{F}(\mathbf{r}) \times \hat{\boldsymbol{\Phi}}_n(\mathbf{r}) \right\rangle}{\left\langle \hat{\boldsymbol{\Phi}}^{\dagger}_m(\mathbf{r}) \middle| \mathbf{F}(\mathbf{r}) \times \hat{\boldsymbol{\Phi}}_m(\mathbf{r}) \right\rangle} X_n(t)$$

$$\frac{\mathrm{d}I_m(t)}{\mathrm{d}t} = \frac{\gamma_I}{\nu Q_m k_{eff}} P_m(t) - \lambda_I I_m(t) \tag{25}$$

$$\frac{\mathrm{d}X_m(t)}{\mathrm{d}t} = \lambda_I I_m(t) + \frac{\gamma_X}{Q_m \nu k_{eff}} P_m(t) \tag{26}$$

$$- \sigma_{a,X} \sum_{n=0}^{N} \frac{\left\langle \hat{\Phi}_m^{\dagger}(\mathbf{r}) \left| \mathbf{T}_{th} X_{eq}(\mathbf{r}) \times \hat{\Phi}_n(\mathbf{r}) \right\rangle}{\left\langle \hat{\Phi}_m^{\dagger}(\mathbf{r}) \left| \hat{\Phi}_m(\mathbf{r}) \right\rangle} P_n(t)$$

$$- \lambda_X X_m(t) - \sigma_{a,X} \sum_{n=0}^{N} Q_n \frac{\left\langle \hat{\Phi}_m^{\dagger}(\mathbf{r}) \left| \phi_{eq,2}(\mathbf{r}) \mathbf{F}(\mathbf{r}) \times \hat{\Phi}_n(\mathbf{r}) \right\rangle}{\left\langle \hat{\Phi}_m^{\dagger}(\mathbf{r}) \left| \hat{\Phi}_m(\mathbf{r}) \right\rangle} X_n(t)$$

Where $\Lambda_{m,n} = \frac{\left\langle \hat{\Phi}_m^{\dagger}(\mathbf{r}) \left| \mathbf{F}(\mathbf{r}) \times \hat{\Phi}_n(\mathbf{r}) \right\rangle}{\left\langle \hat{\Phi}_m^{\dagger}(\mathbf{r}) \left| \mathbf{v} \times \hat{\Phi}_n(\mathbf{r}) \right\rangle}$ and it is assumed that $\Lambda_{mn} \ll \Lambda_{mm}$ for $m \neq n$. For simplicity, $\Lambda_{m,m}$ is written as Λ_m. The above set of ODEs is much simpler to solve numerically than the original PDE system.

2.2. Time-integration analysis

Since the neutron dynamics evolve on a much faster timescale than the iodine and xenon decay, the system of coupled ODEs is stiff. This requires the use of solvers capable of handling stiff systems. The built-in solver ODE15s in MATLAB is used to numerically solve this system of equations. The numerical time-integration of Eqs. (25) to (26) yields three time signals for each mode. Combining these with the spatial modes via Eqs. (21) to (23) returns an approximation of the space- and time-dependence of the change in neutron fluxes, xenon and iodine concentrations after a perturbation. The approximated change in flux can be used to compute the relative changes in reactor power and axial offset (AO), defined as:

$$\delta P(t) = \int_V \left(\kappa \Sigma_{f,1}(\mathbf{r}) \delta\phi_1(\mathbf{r},t) + \kappa \Sigma_{f,2}(\mathbf{r}) \delta\phi_2(\mathbf{r},t) \right) d^3\mathbf{r} \tag{27}$$

$$\delta AO(t) = \frac{\delta P_t(t) - \delta P_b(t)}{\delta P_{max}} \tag{28}$$

Where δP_t and δP_b are the power changes at the top half and bottom half of the reactor, respectively, and δP_{max} is the maximum power change. κ represents the average energy release per fission event. Since the total power level after the transient is unknown, focus is put on the dynamics of deviations from the equilibrium power and axial offset instead.

2.3. Analytical approximation of mode behaviour

Leveraging the ROM's simpler nature, the behaviour of the individual modes without coupling is examined analytically to retrieve approximate stability features of the system. This complements the analysis of the global system behaviour obtained from the superpositions of the modes and may give greater insights into the development of xenon oscillations in specific core configurations. Eqs. (25) to (26) are thus simplified by neglecting the terms in the sums where $m \neq n$ and the following exponential forms are assumed for the solutions:

$$P_m(t) = A_m \cdot \exp\left(\omega_m \cdot t\right) \tag{29}$$

$$I_m(t) = B_m \cdot \exp\left(\omega_m \cdot t\right) \tag{30}$$

$$X_m(t) = C_m \cdot \exp\left(\omega_m \cdot t\right) \tag{31}$$

Utilising these approximations, Eqs. (25) to (26) are written in the following simplified matrix form:

$$\begin{bmatrix} C_{m,11} - \omega_m & 0 & C_{m,13} \\ C_{m,21} & C_{m,22} - \omega_m & 0 \\ C_{m,31} & C_{m,32} & C_{m,33} - \omega_m \end{bmatrix} \begin{bmatrix} A_m \\ B_m \\ C_m \end{bmatrix} = \begin{bmatrix} 0 \\ 0 \\ 0 \end{bmatrix} \tag{32}$$

The only non-trivial solution to this system of equations is found when the determinant of the matrix is zero. This is achieved by solving the following third-order equation for ω_m:

$$\begin{vmatrix} C_{m,11} - \omega_m 0 & C_{m,13} \\ C_{m,21} & C_{m,22} - \omega_m & 0 \\ C_{m,31} & C_{m,32} & C_{m,33} - \omega_m \end{vmatrix} = 0 \tag{33}$$

Solving the above equation results in three roots for each of the N modes included in the model. The first root is related to the prompt neutron behaviour of the system and will not be included in this analysis due to its minor relevance to the stability of xenon oscillations. The two remaining roots are related to the xenon-iodine behaviour, and they are complex numbers. The real part is also called the stability coefficient and determines the exponential growth (positive) or decay rate (negative) of the mode amplitude. The imaginary part is known as the oscillation coefficient and determines the oscillation frequency of the mode. Higher imaginary values correspond to shorter oscillation periods, while a zero imaginary value corresponds to no oscillation.

The analytically calculated mode behaviour provides information which can be used to determine which modes drive the collective behaviour of the system.

Table 1
System parameters.

Parameter	Value
Active core + reflector height	396.24 cm
Active core + reflector volume	$4.05 \cdot 10^7$ cm^3
Active core height	365.76 cm
Active core volume	$2.66 \cdot 10^7$ cm^3
Assembly pitch	21.50 cm
Burnup	919.85 EFPH
Nominal power	3293.3 MW$_{th}$
Power level	99.9% of nominal power
Initial AO	1.4%

Table 2
Physical quantities.

Parameter	Value
λ_I	$3.14 \cdot 10^{-5}$ s^{-1}
λ_X	$2.09 \cdot 10^{-5}$ s^{-1}
γ_I	$6.20 \cdot 10^{-2}$
γ_X	$2.00 \cdot 10^{-3}$
σ_X	$1.30 \cdot 10^{-18}$ cm^2
ν	2.44
κ	$2.98 \cdot 10^{-11}$ J

3. Case study

This section describes the case study considered hereafter and details the data preparation needed for the modal ROM. The investigated three-dimensional reactor system is representative of an actual core configuration of the Ringhals-4 PWR. A radial representation of the core burnup is seen in Fig. 1.

The investigated three-dimensional reactor system is representative of an actual core configuration of the Ringhals-4 PWR. The system consists of an active core region and a reflector region with characteristics summarised in Table 1. The unit EFPH (Effective Full Power Hours) is used to quantify the operational time or burnup of the reactor. The values of the remaining physical quantities needed to describe the reactor system are described in Table 2.

With AO being the axial offset defined as the difference between top and bottom power over the total power $AO = \frac{P_t - P_b}{P_{tot}}$. The nodal cross-section data are derived from plant-specific data provided by the core analysis, fuel, and safeguards group at the Ringhals nuclear power plant using SIMULATE-5 (Vanevenhoven et al., 2022). The cross-sections are initially generated with a spatial resolution of 34 × 34 × 26 nodes in the x, y and z directions, which is refined to 68 × 68 × 52 by duplication. The mesh refinement aims to enhance the accuracy of the eigenvalue solver by minimising spatial discretisation errors.

The CORE SIM solver (Demazière, 2011) is used to calculate the spatial eigenmodes and the corresponding λ-eigenvalues of the heterogeneous system, as well as their adjoints. For the case study, five modes were included in the model, i.e., the fundamental mode, the modes corresponding to the first and second-order axial harmonics, and the two first-order radial harmonics. A schematic of these modes is shown

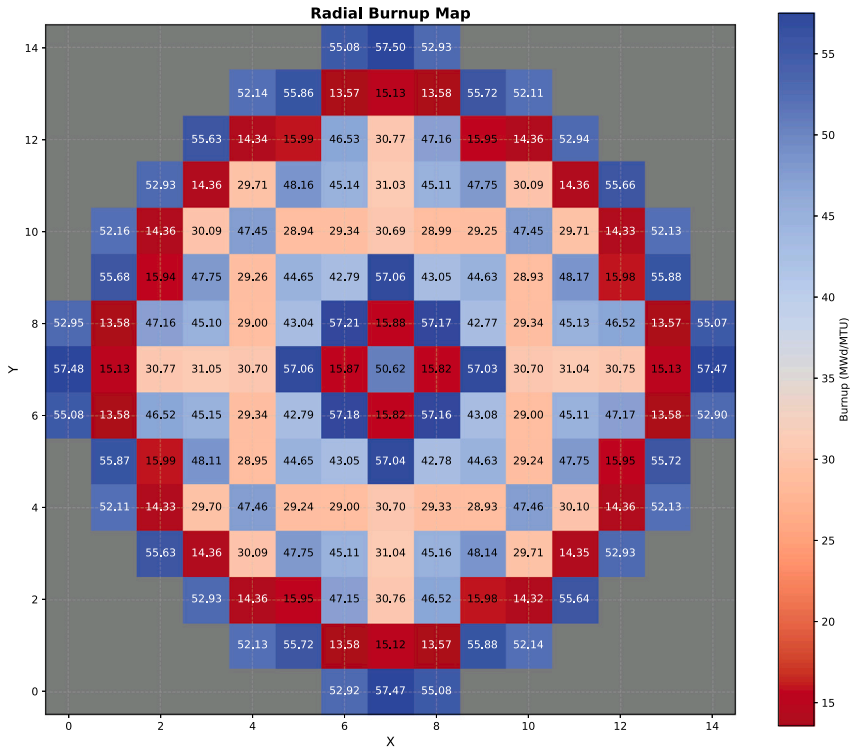

Fig. 1. Burnup map of the Ringhals-4 PWR reactor used in the case study.

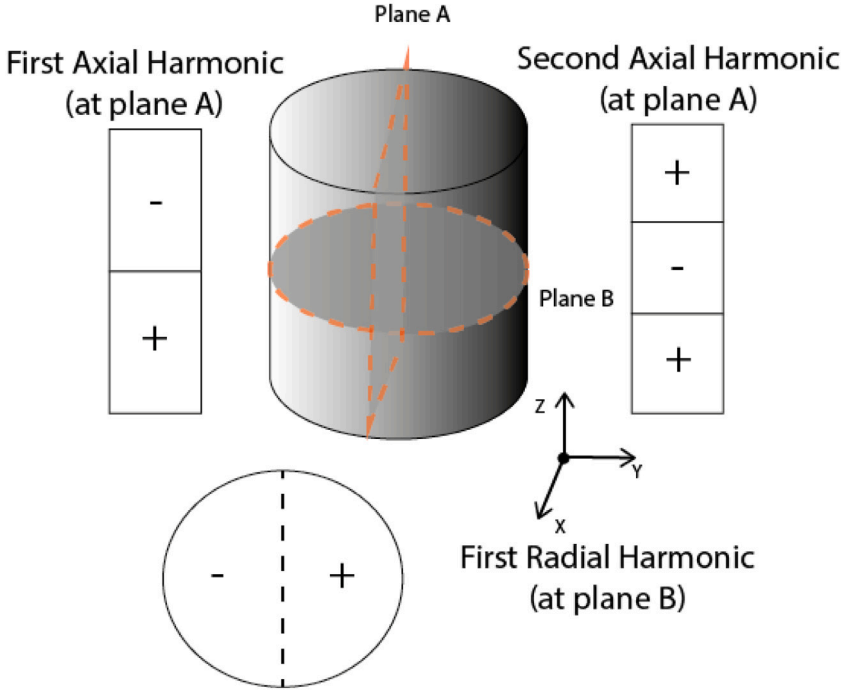

Fig. 2. Schematics of the first axial and radial harmonics and second axial harmonic of the system. The positive and negative deviations of the flux from its static value for the different modes are indicated by plus and minus signs, respectively. The orange dotted lines represent the axial and radial planes. Based on (Obaidurrahman and Singh, 2010).

in Fig. 2. A higher number of spatial modes was considered but was found not to give any additional information.

To solve the ODE system in Eqs. (25) to (26), a set of $3N$ initial conditions are given. These conditions impose a value for the amplitude of each mode at $t = 0$. It follows from Eqs. (21) to (23) that the combination of initial amplitudes corresponds to an initial state of the neutron flux, iodine and xenon concentration fields. The initial conditions need to be non-zero to create a perturbed non-equilibrium state that avoids a trivial solution. The conditions are chosen to emphasise axial offset at the start of the time integration. The initial value of the amplitude corresponding to the first axial harmonic mode of the neutron flux is set to $3 \cdot 10^{14}$ cm^{-2} s^{-1} or half of the full-power static flux. All other

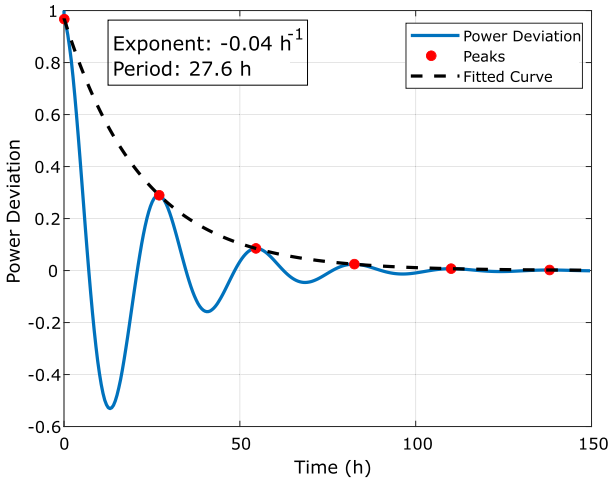

Fig. 3. Predicted change in power as calculated by 2G-HET.

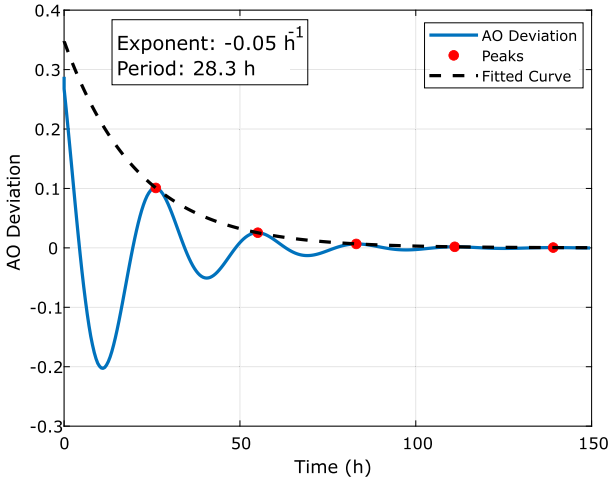

Fig. 4. Predicted change in axial offset as calculated by 2G-HET.

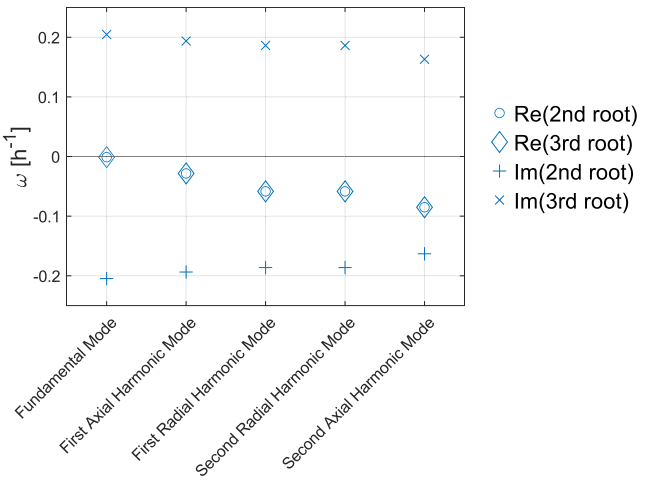

Fig. 5. Real (diamond and circle) and imaginary (crosses and plusses) parts of the second and third roots for each mode in 2G-HET. These real and imaginary values are equivalent to the stability and oscillation coefficients of the modes, respectively. The stability coefficient for the fundamental mode is negative.

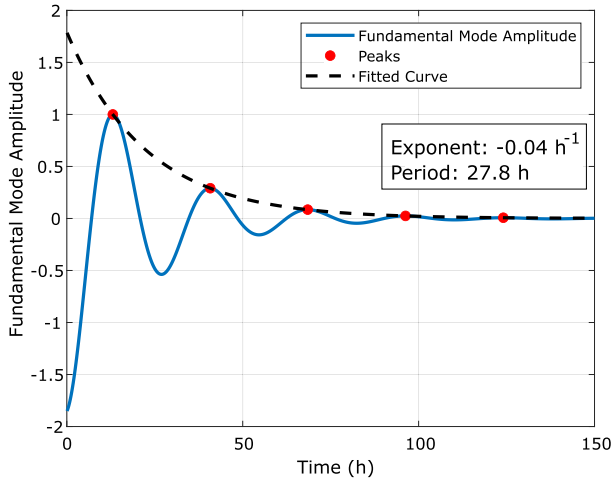

Fig. 6. Amplitude of the fundamental mode of the neutron flux calculated by 2G-HET.

amplitudes are set to fixed random non-zero values in the interval $[-6;6]\cdot 10^{9}\ \mathrm{cm}^{-2}\ \mathrm{s}^{-1}$ equivalent to ±1 pcm of the static flux. The model was tested using different initial conditions, but this did not affect the results.

4. Analysis results

The modal ROM is applied to the system described above. First, the results of the heterogeneous model (2G-HET) are presented. Second, a homogeneous model (2G-HOM) is introduced to evaluate the effect of spatial refinement of the model parameters. Lastly, the two models are compared in terms of their stability prediction and individual mode behaviour to assess the effect of homogenisation.

4.1. ROM-based stability analysis

The time series of the power and axial offset deviations are calculated from the combination of the 2G-HET model Eqs. (25)–(26), Eqs. (21)–(23), and Eqs. (27)–(28), and are shown in Figs. 3 and 4, respectively.

The peak amplitudes are identified and fitted with an exponential function to estimate the exponential constant corresponding to the stability coefficient of the system. The period of oscillation is calculated as the average distance between the adjacent peak amplitudes. The power deviation predicted by 2G-HET oscillates with a period of 27.6 hours and decays with a exponential constant of $-4\cdot 10^{-2}\,\mathrm{h}^{-1}$. The axial offset oscillates with a period of 28.3 h and has an exponential constant of $-5\cdot 10^{-2}\,\mathrm{h}^{-1}$.

Fig. 5 shows the roots of the individual modes calculated from Eq. (33) for the 2G-HET model. As discussed in Section 2.3, only the second and third roots associated with the iodine and xenon concentrations are considered. This analysis shows that the stability coefficient of all roots is negative, with the fundamental mode having the least negative value stability coefficient ($-10^{-3}\,\mathrm{h}^{-1}$) and the higher modes having more negative values in the interval $[-9;-2]\cdot 10^{-2}\,\mathrm{h}^{-1}$. The oscillation coefficient of all roots is non-zero and in the interval $\pm[1.6;2]\cdot 10^{-1}\,\mathrm{h}^{-1}$ equivalent to an oscillation period between 31.5 and 39.3 hours. These results indicate a dampened oscillatory behaviour for all modes.

From the results in Figs. 5, it is hypothesised that the fundamental mode, with the lowest exponential coefficient, drives the oscillations in the first and second axial harmonic mode. Because of this, the symmetric fundamental mode should also be the main driver of the power oscillations. The calculated exponential constant without the effect of couplings does not directly match the observed exponential constant of the power. However, when mode coupling is accounted

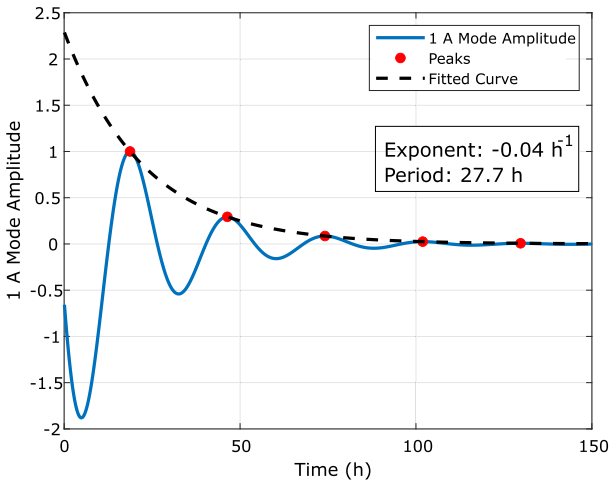

Fig. 7. Amplitude of the first axial harmonic mode of the neutron flux calculated by 2G-HET. "1 A Mode" refers to the first axial harmonic mode.

for in the amplitude calculations, the fundamental mode exhibits oscillation and decay characteristics that align closely with the power deviation, as can be noticed by comparing Figs. 3 and 6. Similarly, the first axial harmonic mode, together with its coupling to the other modes, describes most of the behaviour of the axial offset, as can be seen by comparing Figs. 4 and 7. The discrepancies are small and may be due to the effects of oscillations in the fundamental mode. These results suggest that the interaction between modes plays an important role in both power and axial offset oscillations.

4.2. Comparison with a fully homogenised model

Earlier work by Song et al. (1999) developed an analytical one-dimensional fully homogenised model of the xenon-iodine dynamics. The model is based on modal decomposition but is simplified by studying the axial difference parameters instead of the local neutron flux, iodine and xenon population. The model performs well when compared to modelled and experimental benchmark data following a simple axial perturbation of the axial flux. The success of this model gives motivation to compare a two-group three-dimensional homogenised model based on modal decomposition against its more complex heterogeneous counterpart. This section presents the development of a simplified version of the modal ROM, namely 2G-HOM. The model builds on the Eqs. (25) to (26) but utilises a set of homogenised cross sections and spatial functions, calculated as analytical solutions to the three-dimensional Helmholtz equation for a cylindrical system.

The purpose of developing a homogenised model is to investigate the effects of homogenisation on the predictions of the modal ROM. The homogenised model is then compared both to existing literature and to 2G-HET.

4.2.1. Development of the two-group homogenised model (2G-HOM)

The starting point of the homogenisation is the nodal cross-section data from the Ringhals-4 PWR, which is also used as a basis for 2G-HET. The homogenisation of the cross sections is done in four steps to preserve the physical properties of the system, i.e., reaction rates, leakage rates and consequently k_{eff}.

In the first step, the spatial nodes of the cross sections are split into two categories. One is the group of nodes belonging to the active core in which $\Sigma_{f,g} \neq 0$; the other is the group of nodes belonging to the reflector region where no fission occurs. These two regions of nodes are homogenised using the following formula:

$$\Sigma_{\alpha,g,I} = \frac{\sum_i \Sigma_{\alpha,g,i}\phi_{g,i}}{\sum_i \phi_{g,i}} \quad \text{for } i \in I \tag{34}$$

Where the index i denotes the homogenised micro-region in the heterogeneous model belonging to macro-region I in the fully homogenised model. The subscript α denotes the specific reaction, and g is the energy group.

In the second step, the size of the homogenised reflector region is tuned to account for the cylindrical approximation of the core and to preserve leakage rates.

In the third step, the two regions are homogenised into one.

In the fourth step, k_{eff} is calculated and compared to the value of the heterogeneous system. Steps two to four are iterated until the value for k_{eff} matches with the one of 2G-HET, and similar physical properties are ensured. The eigenfunctions of the homogenised system are calculated analytically as the solution to the Helmholtz equation for a cylindrical system, as described below.

It is assumed that the analytical solution to the neutron flux can be separated into its spatial components as follows:

$$\phi(z,r,\theta) = Z(z)R(r)\Theta(\theta) \tag{35}$$

The individual solutions for the axial components are described in the following two steps:

1. Calculate $B_{z,n}$ as:

$$B_{z,n} = \begin{cases} \frac{\pi}{H} & \text{if } n = 0, \\ \frac{(2\lceil n/2\rceil+1)\pi}{h} & \text{if } n \text{ is even}, \\ \frac{2\lceil n/2\rceil\pi}{h} & \text{if } n \text{ is odd}. \end{cases} \tag{36}$$

where $\lceil x \rceil$ is the ceiling function, which rounds any real number up to the smallest integer that is not less than x.

2. Calculate the axial function $\phi_n(z)$ for a given index n as:

$$Z_n(z) = \begin{cases} \cos\left(B_{z,n}z\right) & \text{if } n \text{ is even}, \\ \sin\left(B_{z,n}z\right) & \text{if } n \text{ is odd}. \end{cases} \tag{37}$$

Likewise, the radial and azimuthal functions given indices m and k, are computed in the following three steps:

1. Calculate $B_{r,z,k}$ as:

$$B_{r,m,k} = \frac{j_{m,k}}{R} \tag{38}$$

where $j_{m,k}$ is the kth zero of the Bessel function $J_m(x)$.

2. Calculate the radial component $(\phi_{m,k}(r))$ given indices m and k as:

$$R_{m,k}(r) = J_{\lceil m/2\rceil}(B_{r,z,k} \cdot r) \tag{39}$$

3. Calculate the azimuthal component $(\Theta_m(\theta))$ given index m as:

$$\Theta_m(\theta) = \begin{cases} 1 & \text{if } m = 0, \\ \sin(\lceil m/2\rceil \cdot \theta) & \text{if } m \text{ is odd}, \\ \cos(\lceil m/2\rceil \cdot \theta) & \text{if } m \text{ is even}. \end{cases} \tag{40}$$

The components of the feedback matrix are calculated in the following two steps:

1. The heterogeneous cross sections are evaluated with SIMULATE-5 for two different power levels and are homogenised using Eq. (34).

2. The power scaling at each power level P_j is calculated as:

$$S_{P,j} = \frac{k_{eff,j} \cdot P_j}{\int_V \kappa_{1,j}(\mathbf{r})\phi_{1,j}(\mathbf{r}) + \kappa_{2,j}(\mathbf{r})\phi_{2,j}(\mathbf{r})d^3\mathbf{r}} \tag{41}$$

Using this, the feedback coefficient for each reaction α is calculated as:

$$K_{\alpha,g} = \frac{S_{P,2}\Sigma_{\alpha,g,2} - S_{P,1}\Sigma_{\alpha,g,1}}{S_{P,2} - S_{P,1}} \tag{42}$$

Table 3
Eigenvalue separation comparison between the models.

	1st Axial	1st Radial	2nd Radial	2nd Axial
2G-HET	579 pcm	953 pcm	953 pcm	2153 pcm
2G-HOM	283 pcm	1430 pcm	1430 pcm	754 pcm
Difference	296 pcm	−477 pcm	−477 pcm	1399 pcm

and for the leakage rate as:

$$K_{\mathbf{J},g} = B^2 \frac{S_{P,2} D_{g,2} - S_{P,1} D_{g,1}}{S_{P,2} - S_{P,1}} \tag{43}$$

with $B^2 = B^2_{z,0} + B^2_{r,0,0}$ being the geometric buckling of the system. The feedback matrix elements are finally arranged as:

$$\mathbf{K}_{th} = \begin{bmatrix} K_{f,1} - K_{\mathbf{J},1} - K_{a,1} - K_r & K_{f,2} \\ K_r & -K_{\mathbf{J},2} - K_{a,2} \end{bmatrix} \tag{44}$$

4.2.2. Comparison between 2G-HOM and 2G-HET

This section compares the eigenvalue separation (EVS), analytical mode roots, coupling strength, power, and axial offset between the 2G-HET and 2G-HOM models. Differences in inter-mode couplings are explained using the axial profile of the coupling terms.

The eigenvalue separation (EVS) is defined as the difference in eigenvalue between the fundamental mode and higher modes in the system expansion, i.e.

$$EVS = \frac{1}{\lambda_m} - \frac{1}{\lambda_0} \quad m = 0, 1, 2, \ldots, N \tag{45}$$

Low EVS values are typical of systems more prone to instabilities, as they reflect weaker mode separation and potentially stronger inter-mode interactions (Obaidurrahman and Singh, 2010). The EVS is explicitly present in the first term of the right-hand side of Eq. (25). The eigenvalues are strongly tied to the dimensions of the core, which impact the spatial neutronic coupling within the core. In Table 3, EVS values are compared for the four higher 2G-HET and 2G-HOM modes. For the first and second axial harmonic modes, EVS is larger in 2G-HET, indicating greater mode separation. Conversely, for the first and second radial modes, EVS is larger in 2G-HOM, suggesting different contributions of these modes to the overall system stability. This indicates that EVS contributes differently to inherent stability predictions for axial harmonic modes than radial harmonic modes in the two models.

To further investigate the difference between the two models, the FB-scaling of the feedback matrix is varied. The FB-scaling is defined as a scalar value multiplied by the feedback matrix in (44) to produce a new feedback matrix:

$\mathbf{K}_{th,new} = \text{FB-scaling} \cdot \mathbf{K}_{th}$. Fig. 8 illustrates the real part of the two roots for the fundamental mode (namely, the 2nd and 3rd roots) as a function of this scaling. In addition, it marks in dash-dotted lines the values of FB-scaling for which the imaginary parts of the roots become zero and the real parts bifurcate. The oscillation occurs when the two real parts are identical, and two non-zero imaginary values with opposite signs exist. Thus, the physical significance of this point is that the mode no longer oscillates past the bifurcation, and two stability coefficients exist. After the bifurcation one root will have larger value than the other. One of the 2G-HOM roots has less negative value than the roots of the 2G-HET before bifurcation. The values that the 2G-HET roots converge to after bifurcation is not examined as only the points of bifurcation where oscillations occur are of interest.

As seen in Fig. 8, both models exhibit strong increases in stability coefficient for lower values of FB-scaling. Conversely, the values saturate between $-0.1\ \text{h}^{-1}$ and $-0.3\ \text{h}^{-1}$ for increasing FB-scaling. The stability coefficient of 2G-HOM is more negative, compared to 2G-HET, for FB-scaling smaller than 10.

It is of interest to investigate the FB-scaling factor for which the stability coefficient of the analytical analysis without coupling becomes

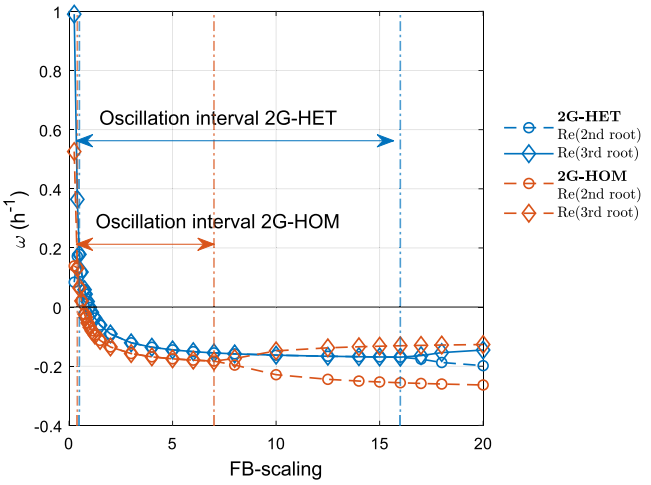

Fig. 8. Comparison of the analytically calculated stability coefficient between the 2G-HOM model and 2G-HET model. Dashed lines indicate the point of bifurcation of the stability coefficient.

positive for each mode, thus identifying the onset of unstable behaviour. Fig. 9 compares these values between 2G-HET and 2G-HOM. For all modes in 2G-HET, higher FB-scaling values are required to achieve stability compared to 2G-HOM. As only one unstable mode is required to make the whole system unstable, it is concluded that 2G-HOM requires a 25% lower FB-scaling value to achieve stability (0.75) compared to 2G-HET (1).

This indicates that 2G-HET demands stronger thermal feedback to predict a stable system. The analytical roots of the 2G-HET and 2G-HOM models, using the nominal feedback values and without coupling between modes, are compared in Fig. 10. The analysis shows that 2G-HOM have larger negative values of the stability coefficients for all modes. This indicates that the modes without the effect of coupling have a faster exponential decay for 2G-HOM compared to 2G-HET. The oscillation coefficients of 2G-HOM are smaller compared to 2G-HET for all modes. As a result, 2G-HOM exhibits longer oscillation periods.

To better understand the effect of heterogeneities on the coupling terms, the following spatially dependent quantities are first introduced:

$$\text{FB}_{m,n}(\mathbf{r}) = \frac{1}{\Lambda_m} \frac{\hat{\boldsymbol{\Phi}}^\dagger_m(\mathbf{r}) \cdot \mathbf{K}_{th} \times \hat{\boldsymbol{\Phi}}_n(\mathbf{r})}{\left\langle \hat{\boldsymbol{\Phi}}^\dagger_m(\mathbf{r}) \middle| \mathbf{F}(\mathbf{r}) \times \hat{\boldsymbol{\Phi}}_m(\mathbf{r}) \right\rangle} \tag{46}$$

$$\text{P1}_{m,n}(\mathbf{r}) = \frac{Q_n}{\Lambda_m} \frac{\hat{\boldsymbol{\Phi}}^\dagger_m(\mathbf{r}) \cdot \phi_{eq,2}(\mathbf{r}) \mathbf{F}(\mathbf{r}) \times \hat{\boldsymbol{\Phi}}_n(\mathbf{r})}{\left\langle \hat{\boldsymbol{\Phi}}^\dagger_m(\mathbf{r}) \middle| \mathbf{F}(\mathbf{r}) \times \hat{\boldsymbol{\Phi}}_m(\mathbf{r}) \right\rangle} \tag{47}$$

$$\text{X}_{m,n}(\mathbf{r}) = \frac{\hat{\boldsymbol{\Phi}}^\dagger_m(\mathbf{r}) \mathbf{T}_{th} X_{eq}(\mathbf{r}) \times \hat{\boldsymbol{\Phi}}_n(\mathbf{r})}{\left\langle \boldsymbol{\Phi}^\dagger_m(\mathbf{r}) \middle| \boldsymbol{\Phi}_m(\mathbf{r}) \right\rangle} \tag{48}$$

$$P2_{m,n}(\mathbf{r}) = Q_n \frac{\hat{\boldsymbol{\Phi}}^\dagger_m(\mathbf{r}) \cdot \phi_{eq,2}(\mathbf{r}) \mathbf{F}(\mathbf{r}) \times \hat{\boldsymbol{\Phi}}_n(\mathbf{r})}{\left\langle \hat{\boldsymbol{\Phi}}^\dagger_m(\mathbf{r}) \middle| \hat{\boldsymbol{\Phi}}_m(\mathbf{r}) \right\rangle} \tag{49}$$

for $m, n = 0, 1, 4$. The spatial integration Eqs. (46) to (49) correspond to the terms appearing in the ROM balance Eqs. (25) to (26) and are given in Table 4.

Only couplings between the fundamental mode and higher axial harmonic modes are shown in Table 4 as no non-zero couplings exist between the higher radial harmonic modes included in the model. The couplings between the fundamental mode and the first axial harmonic are only non-zero for 2G-HET. This results from the axial offset resolved in the model, which is exemplified in Fig. 11. The figure shows the normalised axial profile of the $\text{P2}_{0,1}$ coupling term between the fundamental mode and the first axial harmonic mode. The axial profile of 2G-HOM is completely antisymmetric, leading to a null result upon

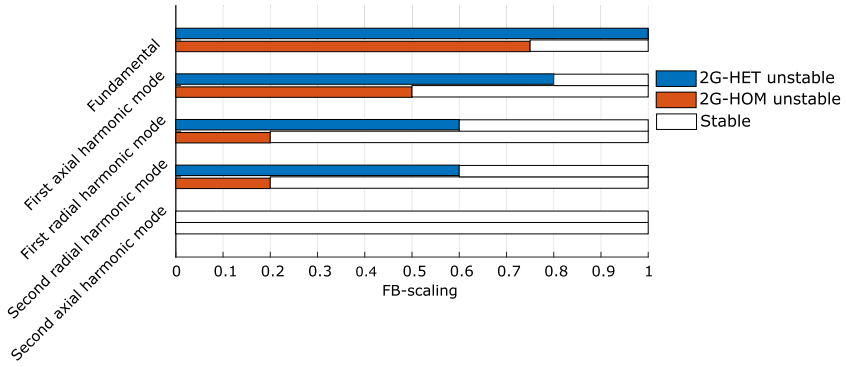

Fig. 9. Stability of each mode as a function of the FB-Scaling. Comparison between 2G-HET (blue) and 2G-HOM (red).

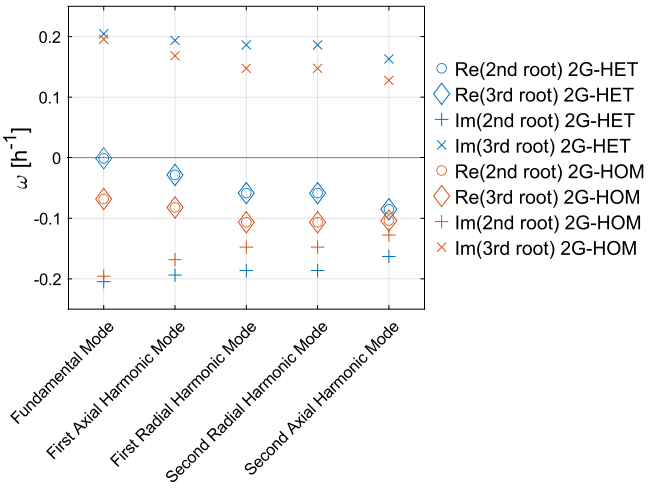

Fig. 10. Comparison of the modes of the real (circles and diamonds) and imaginary (crosses and plusses) parts of the second and third root of the 2G-HET (blue) and 2G-HOM (red). The real and imaginary values are equivalent to the stability coefficients and oscillation coefficients, respectively.

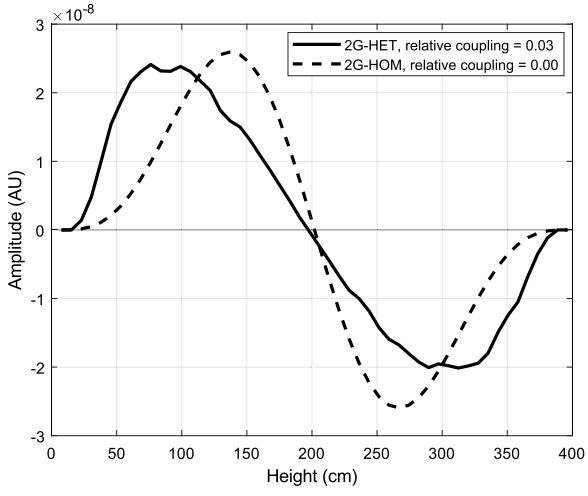

Fig. 11. Normalised axial profile of the coupling function $P2_{0,1}$ between the fundamental mode and first axial harmonic mode compared between 2G-HET and 2G-HOM. "Relative coupling" in the legend refers to the integral of each of the profiles.

Table 4
Comparison of the integrals of Eqs. (46) to (49) between 2G-HET and 2G-HOM for different combinations of modes. In the "Coupling" column, F refers to the fundamental mode (m,n = 0), 1st refers to the first axial harmonic mode (m,n = 1) and 2nd refers to the second axial harmonic mode (m,n = 4).

	$FB_{m,n}$		$P1_{m,n}$		$X_{m,n}$		$P2_{m,n}$	
Coupling	HET	HOM	HET	HOM	HET	HOM	HET	HOM
F → F	1.00	1.00	1.00	1.00	1.00	1.00	1.00	1.00
F → 1st	0.06	0.00	0.03	0.00	−0.01	0.00	0.03	0.00
F → 2nd	0.15	0.00	0.06	0.20	0.01	0.06	0.06	0.20
1st → F	0.10	0.00	0.05	0.00	−0.02	0.00	0.06	0.00
1st → 1st	0.85	1.00	0.94	0.80	0.99	0.94	0.94	0.80
1st → 2nd	−0.07	0.00	−0.03	0.00	0.01	0.00	−0.03	0.00
2nd → F	0.25	0.00	0.10	0.20	0.01	0.06	0.10	0.20
2nd → 1st	−0.10	0.00	−0.03	0.00	0.01	0.00	−0.03	0.00
2nd → 2nd	0.76	1.00	0.95	0.77	0.98	0.91	0.94	0.77

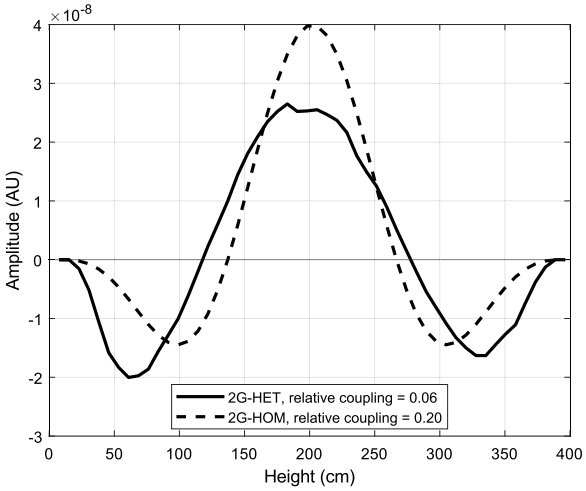

Fig. 12. Normalised axial profile of the coupling function $P2_{0,4}$ between the fundamental mode and the second axial harmonic mode compared between 2G-HET and 2G-HOM. "Relative coupling" in the legend refers to the integral of each of the profiles.

integration. In contrast, the axial profile of 2G-HET exhibits skewness, leading to a non-zero result of 0.03 upon integration. Consequently, the sign of the coupling between the fundamental mode and the first axial harmonic depends on the sign of the axial offset in the equilibrium flux distribution. Xenon oscillations have frequently been investigated using simplified geometries, such as slab reactors or two-point cylindrical models, as seen in the studies by Gyorey (1962), Canosa and Brooks (1966). While these approaches provide valuable insight under idealised and highly symmetric conditions, their limited spatial resolution

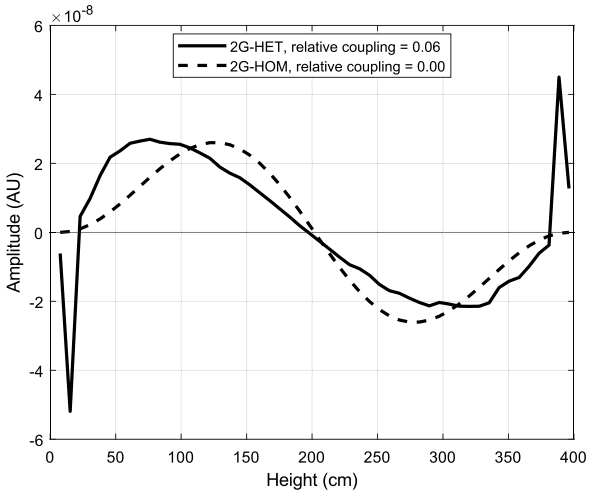

Fig. 13. Normalised axial profile of the coupling function $FB_{0,1}$ between the fundamental mode and the first axial harmonic mode compared between 2G-HET and 2G-HOM. "Relative coupling" in the legend refers to the integral of each of the profiles.

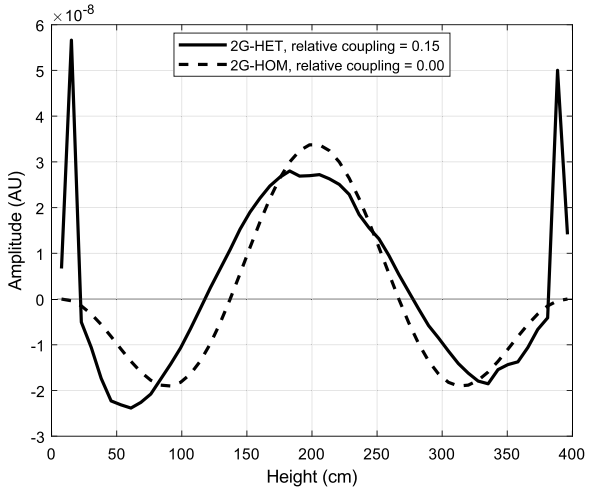

Fig. 14. Normalised axial profile of the coupling function $FB_{0,4}$ between the fundamental mode and the second axial harmonic mode compared between 2G-HET and 2G-HOM. "Relative coupling" in the legend refers to the integral of each of the profiles.

may obscure mode interactions. In contrast, the higher resolution of the core-reflector system in the present work reveals couplings between even and odd modes that are not captured in these models. Fig. 12 presents the normalised axial profile of the $P2_{0,4}$ coupling term, which describes the interaction between the fundamental mode and the second axial harmonic mode. Owing to the symmetry of these modes and the equilibrium flux, the central peak of the profile is more pronounced than the two peaks in the negative region. As a result, the overall integral yields a positive value. The coupling strength between even harmonic modes is lower in 2G-HET than in 2G-HOM due to the flatter equilibrium flux profile in this model. This result is consistent with (Gyorey, 1962). While the axial offset also influences this coupling, the dominant factor is the flatness of the equilibrium flux distribution. Figs. 13 and 14 show that the heterogeneous feedback is affected not only by the axial offset and flatness of the flux but also by the reflection of the neutrons at the edges of the core. The peak at the bottom of the core is a result of the homogeneous treatment of the feedback coefficients. In a heterogeneous treatment, the power coefficient of reactivity is not expected to have any influence below the active core region. In the above analysis of heterogeneous effects on the coupling between modes, only the axial profiles were considered because no radial offset was present in the reactor.

The 70-h power and AO deviation predictions of 2G-HET and 2G-HOM are compared in Figs. 15(a) and 15(b). The behaviour of the collective system exhibits slower convergence and shorter periods for 2G-HET compared to 2G-HOM. This is consistent with the findings of the analysis of the individual modes.

5. Conclusion and outlook

In this work, a modal reduced-order model (2G-HET) was proposed to predict the stability of a PWR system regarding xenon oscillations. The model took three-dimensional two-energy group macroscopic cross sections and the physical dimensions of the reactor as input. It calculated the spatial eigenmodes as well as three time-dependent amplitudes for each mode, associated with the evolution of the neutron flux, iodine, and xenon concentration, respectively. The model was studied using cross sections generated from the Ringhals-4 PWR. The deviation of the power and axial offset from equilibrium was calculated from the output, and the oscillation characteristics were investigated. The analysis of the behaviour of the modes, including and excluding their possible coupling between the modes, was utilised to gain further physical insights.

The predicted evolution of the fundamental mode and the first axial harmonic mode, both with and without coupling, was compared to the power and axial offset predictions, respectively. The analysis showed a much stronger correlation between the fundamental mode and power deviation, as well as between the first axial harmonic mode and axial offset deviation, when couplings were included. This indicated that the coupling between modes played a significant part in the final power and axial offset deviation predictions.

A second model (2G-HOM), utilising a set of cross-sections homogenised over the entire core and reflector region, as well as analytically calculated eigenmodes, was developed to assess the effect of homogenisation on the model results.

The two models were compared in terms of eigenvalue separation and mode behaviour, excluding the effect of coupling, over a range of thermal feedback strengths and the relative coupling strength between modes. Lastly, predictions for power and axial offset deviations were compared.

Compared to 2G-HET, the 2G-HOM model predicted faster decay rates and longer oscillation periods for power and axial offset deviations, driven by larger negative stability coefficients for all modes. 2G-HET required a larger negative feedback coefficient to be stable for all modes when varying the thermal feedback scaling within the oscillatory limits of the model.

Interestingly, the results showed that resolving the neutron axial offset of the core gave rise to couplings between even and odd modes, which was not observed in the symmetric homogeneous core. The findings underscored the importance of capturing spatially resolved mode couplings when predicting xenon-induced stability. Neglecting such couplings, as in 2G-HOM, may have resulted in predictions of behaviour which varied significantly compared to the case where they were included.

The model was based on linear diffusion theory, i.e., non-linearities were not included. This approximation was expected to be sufficient to predict the behaviour of the core when the oscillations were small and to establish the sign of the stability coefficient of free-running xenon oscillations, which was the most important task for the model. Extending the model to scenarios involving larger perturbations or nonlinear interactions may require incorporating higher-order terms in the underlying equations.

To assess the reliability and accuracy of the 2G-HET model, comparisons against industry-like methodologies will be an important next

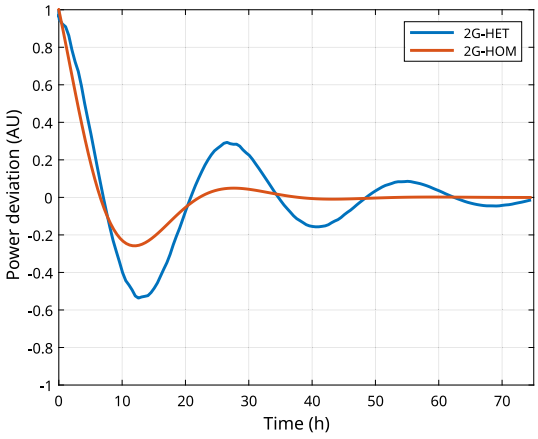

(a) Power deviation response predicted by 2G-HET and 2G-HOM

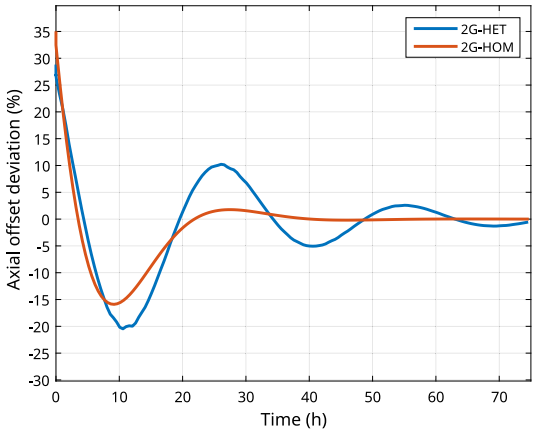

(b) Axial offset deviation response predicted by 2G-HET and 2G-HOM.

Fig. 15. Comparisons of power (left) and axial offset (right) between 2G-HET and 2G-HOM.

step. Additionally, investigating different scenarios, including varying burnup levels, fuel cycle, and reactor designs, will allow for an evaluation of the robustness and ability to generalise the model. The effect of a heterogeneous treatment of the power coefficient of reactivity on the coupling between modes requires further investigation. Ultimately, the model will make it possible to predict whether a core is stable or unstable with respect to xenon oscillations, based on the sole knowledge of the core loading and the corresponding macroscopic cross-section data. The three-dimensional implementation and inclusion of multi-mode coupling allow the model to be extended to systems experiencing azimuthal and radial oscillations and, in turn, capture more complex oscillatory behaviour for a wider range of core designs.

CRediT authorship contribution statement

Kristoffer Tofveson Pedersen: Writing – original draft, Visualization, Software, Methodology, Investigation, Formal analysis. **Christophe Demazière:** Writing – review & editing, Supervision, Funding acquisition, Conceptualization. **Paolo Vinai:** Writing – review & editing, Supervision.

Declaration of competing interest

The authors declare that they have no known competing financial interests or personal relationships that could have appeared to influence the work reported in this paper.

Acknowledgements

The Swedish Radiation Safety Authority (SSM) is financing this project with an in-kind contribution to the Swedish Centre for Nuclear Technology (SKC) (contract number SSM2019-729).

The authors would like to acknowledge the efforts of the core analysis, fuel, and safeguards group at the Ringhals nuclear power plant for data preparation.

During the preparation of this work the authors used ChatGPT 4 in order to improve the readability of the manuscript. After using this tool, the authors reviewed and edited the content as needed and take full responsibility for the content of the published article.

Data availability

The data that has been used is confidential.

References

Bell, G.I., Glasstone, S., 1970. Nuclear Reactor Theory. Van Nostrand Reinhold Company.

Canosa, J., Brooks, H., 1966. Xenon-Induced Oscillations. Nucl. Sci. Eng. 26 (2), 237–253. http://dx.doi.org/10.13182/NSE66-A28166, URL: https://www.tandfonline.com/doi/full/10.13182/NSE66-A28166.

Carreño, A., Vidal-Ferràndiz, A., Ginestar, D., Verdú, G., 2017. Spatial modes for the neutron diffusion equation and their computation. Ann. Nucl. Energy 110, 1010–1022. http://dx.doi.org/10.1016/j.anucene.2017.08.018, URL: https://linkinghub.elsevier.com/retrieve/pii/S0306454917300208.

Carreño, A., Vidal-Ferràndiz, A., Ginestar, D., Verdú, G., 2019. Modal methods for the neutron diffusion equation using different spatial modes. Prog. Nucl. Energy 115, 181–193. http://dx.doi.org/10.1016/j.pnucene.2019.03.040, URL: https://linkinghub.elsevier.com/retrieve/pii/S0149197019301052.

Chang, G., 2016. Advanced CANDU reactors axial xenon oscillation controllability validation. Ann. Nucl. Energy 96, 441–445. http://dx.doi.org/10.1016/j.anucene.2016.06.039, URL: https://linkinghub.elsevier.com/retrieve/pii/S0306454916304820.

Christie, A.M., Poncelet, C.G., 1973. On the control of spatial xenon oscillations. Nucl. Sci. Eng. 51 (1), 10–24. http://dx.doi.org/10.13182/NSE73-A23253, URL: https://www.tandfonline.com/doi/full/10.13182/NSE73-A23253.

Demazière, C., 2011. CORE SIM: A multi-purpose neutronic tool for research and education. Ann. Nucl. Energy 38 (12).

Demazière, C., 2017. Physics of Nuclear Reactors (Lecture notes). Chalmers University of Technology, Gothenburg.

G. Verdú, V.V., Miró, R., 1998. Modal decomposition method for-BWR stability analysis. J. Nucl. Sci. Technol. 35 (8), 538–546. http://dx.doi.org/10.1080/18811248.1998.9733907, arXiv:https://doi.org/10.1080/18811248.1998.9733907.

Graves, W.E., 1970. Experience with xenon oscillations. Nucl. Appl. Technol. 9 (5), 651–661. http://dx.doi.org/10.13182/NT70-A28739, arXiv:https://doi.org/10.13182/NT70-A28739.

Gyorey, G.L., 1962. The effect of modal interaction in the xenon instability problem. Nucl. Sci. Eng. 13 (4), 338–344. http://dx.doi.org/10.13182/NSE62-A26175, arXiv:https://doi.org/10.13182/NSE62-A26175.

Hennig, D., Lange, C., Rizwan-uddin, Dokhane, A., Knospe, A., 2019. Principles for the application of bifurcation theory for the systematic analysis of nuclear reactor stability, Part1: Theory. Prog. Nucl. Energy 115, 231–249. http://dx.doi.org/10.1016/j.pnucene.2019.02.009, URL: https://linkinghub.elsevier.com/retrieve/pii/S0149197019300575.

Hjelmeland, M., Nøland, J.K., Backe, S., Korpås, M., 2025. The role of nuclear energy and baseload demand in capacity expansion planning for low-carbon power systems. Appl. Energy 377, http://dx.doi.org/10.1016/j.apenergy.2024.124366, URL: https://linkinghub.elsevier.com/retrieve/pii/S0306261924017495.

International Atomic Energy Agency, 2018. Non-baseload operation in nuclear power plants: load following and frequency control modes of flexible operation / international atomic energy agency. Technical Report NP-T-3.23, International Atomic Energy Agency.

Kalkkuhl, J., Döring, M., 1993. Modal approximation of xenon oscillations in nuclear reactors — an FEM-based approach. Control Eng. Pract. 1 (5), 791–796. http://dx.doi.org/10.1016/0967-0661(93)90245-M, URL: https://linkinghub.elsevier.com/retrieve/pii/096706619390245M.

Kitcher, E.D., Chirayath, S.S., 2017. A neutron transport and thermal hydraulics coupling scheme to study xenon induced power oscillations in a nuclear reactor. Ann. Nucl. Energy 106, 64–70. http://dx.doi.org/10.1016/j.anucene.2017.03.045, URL: https://linkinghub.elsevier.com/retrieve/pii/S0306454916308933.

Kobayashi, K., Yoshikuni, M., 1982. Analysis of xenon oscillation by coupled reactor model. J. Nucl. Sci. Technol. 19 (2), 107–118. http://dx.doi.org/10.1080/18811248.1982.9734123, arXiv:https://doi.org/10.1080/18811248.1982.973412.

Lee, J.C., 2020. Nuclear Reactor: Physics and Engineering, first ed. Wiley.

Lellouche, G.S., 1962. Space dependent xenon oscillations. Nucl. Sci. Eng. 12 (4), 482–489. http://dx.doi.org/10.13182/NSE62-A26095, arXiv:https://doi.org/10.13182/NSE62-A26095.

Mazaher, M.G., Salehi, A.A., Vosoughi, N., 2020. A new Monte Carlo approach for solution of the time dependent neutron transport equation based on nodal discretization to simulate the xenon oscillation with feedback. Ann. Nucl. Energy 141, 107302. http://dx.doi.org/10.1016/j.anucene.2019.107302, URL: https://linkinghub.elsevier.com/retrieve/pii/S0306454919308126.

Norinder, O., 1963. Two-group Analysis of Xenon Stability in Slab Geometry by Modal Expansion. Technical Report AE-108, AB Atomenergi, Nykoeping (Sweden).

Obaidurrahman, K., Singh, O.P., 2010. Spatial neutronic coupling aspects in nuclear reactors. Nucl. Eng. Des. 240 (10), 2755–2760. http://dx.doi.org/10.1016/j.nucengdes.2010.05.004, URL: https://linkinghub.elsevier.com/retrieve/pii/S0029549310003213.

OECD/NEA, 2021. Technical and economic aspects of load following with nuclear power plants. Nucl. Dev. http://dx.doi.org/10.1787/29e7df00-en.

Peakman, A., Merk, B., Hesketh, K., 2020. The potential of pressurised water reactors to provide flexible response in future electricity grids. Energies 13 (4), 941. http://dx.doi.org/10.3390/en13040941, URL: https://www.mdpi.com/1996-1073/13/4/941.

Persson, J., Andgren, K., Henriksson, H., Loberg, J., Malm, C., Pettersson, L., Sandström, J., Sigfrids, T., 2012. Additional Costs for Load-following Nuclear Power Plants. report 2012:71, Elforsk.

Ritchie, H., Rosado, P., 2020. Electricity mix. Our World Data URL: https://ourworldindata.org/electricity-mix.

Song, J.S., Cho, N.Z., 1997. Two-group, flux-coupled xenon oscillation model with an equation system of axial difference parameters. Nucl. Technol. 119 (2), 105–111. http://dx.doi.org/10.13182/NT97-A35379, URL: https://www.tandfonline.com/doi/full/10.13182/NT97-A35379.

Song, J.S., Cho, N.Z., Zee, S.Q., 1999. Analytic modelling of the xenon oscillation due to control rod movement. J. Korean Nucl. Soc. 31 (1), 80–87.

U.S. Department of Energy, 1993. DOE Fundamentals Handbook. Technical Report DOE-HDBK-1019/1-93, 2, U.S. Department of Energy.

U.S. Nuclear Regulatory Commission, 2011. R325c CE technology cross training. URL: https://www.nrc.gov/docs/ML1125/ML11251A047.pdf.

Utley, E.E., 1972. Letter from Carolina Power and Light Company to the U.S. Atomic Energy Commission on Divergent Axial Xenon Oscillations. Technical Report 50–216, U.S. National Regulatory Commission.

Vanevenhoven, S., Bahadir, T., Grandi, G., Rhodes, J.D., 2022. SIMULATE5 user's manual. Studsvik Scandpower, Wilmington, NC, Version 1.23, SSP-10/438 Rev 17.

Velarde, G., Ahnert, C., Aragonés, J.M., 1978. Analysis of the eigenvalue equations in k, λ, γ, and α applied to some fast- and thermal-neutron systems. Nucl. Sci. Eng. 66 (3), 284–294. http://dx.doi.org/10.13182/NSE78-A27213, URL: https://www.tandfonline.com/doi/full/10.13182/NSE78-A27213.

Verdú, G., Ginestar, D., Vidal, V., Muñoz-Cobo, J., 1994. 3D λ-Modes of the neutron-diffusion equation. Ann. Nucl. Energy 21, 405–421.

Yarbrough, M.B., Liu, Y.S., Paterline, D.L., Hone, M.J., 1997. APOLLO- A One. Dimensional Neutron Diffusion Theory Program. Technical Report, Westinghouse Energy Systems.

Zarei, M., Minuchehr, A., Ghaderi, R., 2017. A semi-analytical treatment of xenon oscillations. Ann. Nucl. Energy 106, 127–135. http://dx.doi.org/10.1016/j.anucene.2017.03.043, URL: https://linkinghub.elsevier.com/retrieve/pii/S0306454917300828.